

## RESEARCH ARTICLE

# Thermoplastic self-healing polymer blends for structural composites: Development of polyamide 6 and cyclic olefinic copolymer blends

D. Perin  | A. Dorigato | A. Pegoretti 

Department of Industrial Engineering and  
INSTM Research Unit, University of  
Trento, Trento, Italy

## Correspondence

D. Perin, Department of Industrial  
Engineering and INSTM Research Unit,  
University of Trento, Via Sommarive  
9, 38123 Trento, Italy.  
Email: [davide.perin-1@unitn.it](mailto:davide.perin-1@unitn.it)

## Abstract

One of the main limitations of high-performance composite materials is failure due to fatigue crack propagation during service. Traditional repair methods can be expensive and time-consuming. For this reason, the research in the field of self-healing composites has considerably increased in the past decade. At this aim, this work is focused on the production of a polyamide 6 (PA6) matrix with self-healing properties. Cyclic olefinic copolymer (COC) was selected as a healing agent and it was melt compounded with PA6. From scanning electron microscope micrographs, it was possible to highlight the immiscibility and the lack of interfacial adhesion between the constituents. The healing efficiency of the system was evaluated by comparing the blends' fracture toughness ( $K_{IC}$ ), both in quasi-static and impact mode, before and after the healing process performed at 140°C by applying a pressure of 0.5 MPa. Through the addition of 30 wt% of COC, the fracture toughness of the virgin samples slightly decreased, passing from 2.3 MPa·m<sup>1/2</sup> of neat PA6 to 2.1 MPa·m<sup>1/2</sup>. However, the presence of the 30 wt% of COC homogeneously distributed within the PA6 matrix led to a healing efficiency of 11% in quasi-static mode and 35% in impact mode.

## KEYWORDS

cyclic olefinic copolymer, fracture toughness, polyamide, polymer blends, self-healing

## 1 | INTRODUCTION

In the twentieth century, polymer composites emerged as a promising class of structural materials,<sup>1</sup> as they are characterized by improved design flexibility and easy manufacturing. Furthermore, composites are characterized by high strength, low density, enhanced durability, fairly low maintenance, and corrosion resistance.<sup>2,3</sup>

On the other hand, one of the major problems related to these materials is the prediction of their life span, and thus their reliability.<sup>4</sup> In fiber-reinforced polymers (FRPs) two main failure mechanisms generally occur under load, that is, interfacial delamination and matrix cracking.<sup>5</sup> These two mechanisms lead to the complete failure of the component, which needs to be substituted or at least repaired. Furthermore, the microcracks developed in the

This is an open access article under the terms of the [Creative Commons Attribution-NonCommercial-NoDerivs](https://creativecommons.org/licenses/by-nc-nd/4.0/) License, which permits use and distribution in any medium, provided the original work is properly cited, the use is non-commercial and no modifications or adaptations are made.

© 2023 The Authors. *Journal of Applied Polymer Science* published by Wiley Periodicals LLC.

core of the composite structures are difficult to be detected and repaired, thus making the repairing operations time-consuming, poorly effective, and labor-intensive. For these reasons, researchers and industries have recently shifted their interest toward a new generation of multifunctional composites with self-healing properties.<sup>6</sup>

The potentialities of self-healing composites are numerous, such as the minimization of the costs correlated to maintenance and repair operations, and the enhancement of the service life, thus improving the overall sustainability of these materials. As reported by Zwaag et al.,<sup>7</sup> three important concepts must be taken into consideration to improve the self-healing efficiency of FRPs: localization, time, and mobility of the healing agent/mechanism. The fourth concept was recently introduced by Utrera-Barrios et al.,<sup>8</sup> that is, the self-healing mechanism utilized. The first concept is related to the position of the damage inside the material and also to the different types of damage that can occur, such as microcrack, surface damage, fiber debonding, or fatigue damage. The second aspect is connected to the time gap between the event causing the damage, the activation of the healing mechanism, and its completion. In general, the time gap should be as low as possible, in order to further increase the service life of the product. The third concept, that is, mobility, is strictly connected to the mechanism meaning that, the higher the mobility of the healing agents, the higher would be the healing efficiency and thus its effectiveness.

From a general point of view, self-healing materials can be divided into two broad categories: extrinsic and intrinsic.<sup>9</sup> In extrinsic self-healing systems, an healing agent is pre-embedded in the polymer matrix, and therefore, a crack propagating in the matrix can trigger the healing mechanism. For example, in a widely investigated self-healing system, capsules containing a liquid uncured resin are dispersed in the polymer matrix. A propagating crack can break the capsules and the contained liquid resin can flow to fill the crack and eventually polymerize if properly activated by a catalyst dissolved in the matrix. Through extrinsic self-healing mechanisms, high healing efficiency can be easily achieved, but two major drawbacks are commonly encountered. First, the introduction of capsules inside a polymer matrix negatively affects the overall mechanical properties of the composite. Second, the self-healing mechanism can be performed one time only, since the broken capsules cannot be restored.<sup>10</sup> On the other hand, in intrinsic self-healing systems, the polymeric matrices themselves heal molecular and macroscopic damage like cracks under external stimuli. The activation of the healing mechanism is strictly connected with the chemistry of the selected healing agent, and in particular, it can be

based on either dynamic covalent<sup>11,12</sup> or non-covalent<sup>13</sup> reversible bonds that can be activated by temperature, electromagnetic radiations, or ionic strength changes. Intrinsic self-healing properties of thermosetting matrices can also be obtained by introducing a thermoplastic healing agent.<sup>14–19</sup> One of the most important advantages in comparison to extrinsic self-healing systems is the fact that the healing process can be performed several times, theoretically, until the degradation of the healing agent after multiple healing processes is reached.<sup>20</sup>

Recent literature papers demonstrated the effectiveness of intrinsic self-healing composites based on the dispersion of thermoplastic healing agents in a thermosetting matrix, the same concept could be utilized also for thermoplastic composite materials (TPC). Currently, the TPC market is mainly driven by the automotive, construction, and aerospace industries, with a global market reaching 17.7 Mt in volume and an economic value of \$86 billion.<sup>21</sup> TPCs are characterized by better processability and lower cost in comparison to composites with thermosetting resins and they can be easily reprocessed in recycling operations. Furthermore, the use of nanofillers enables to obtain elevated mechanical properties with limited filler amounts.<sup>22–26</sup> One of the most widely used matrices in TPCs is PA6 since it has excellent strength and stiffness, low friction, high chemical and wear resistance.<sup>27</sup> Recently, in the work of Wang et al.,<sup>28</sup> the inherently low-notched impact strength of PA6 was tackled through the insertion of ethylene-vinyl acetate-g-glycidyl methacrylate (EVA-GMA). Furthermore, they also investigated the effect on the mechanical and dielectric properties upon the addition of hydroxylated BaTiO<sub>3</sub> and multi-walled carbon nanotubes (MWCNTs). Another remarkable application of PA6 was reported in the recent work of Cheng et al.,<sup>29</sup> in which graphene polyamide blend fibers were used as an effective electrode for supercapacitors.

The major drawbacks of TPCs are generally related to their inherently lower strength and lower thermal stability in comparison to thermosetting FRPs. Repairing operation and re-consolidation of TPCs can be performed either by local melting or using fusion bonding techniques.<sup>30</sup> However, these repairing operations require high temperatures, special molds, and high labor costs, causing in many cases the geometrical distortion of the components. For these reasons, an intrinsic self-healing system embedded within the thermoplastic matrix in TPC could potentially represent a feasible and cost-effective solution to repair these composites. In this way, the service life of these materials could be further enhanced, making them also more sustainable from an environmental point of view.

The investigation of immiscible healing agents embedded in a composite matrix started in 1999, and the majority of these works were conducted on epoxy-based composites, and by using polyethylene-co-methacrylic acid (EMAA) as a healing agent.<sup>31,32</sup> As reported in the literature, EMAA revealed excellent healing behavior even after multiple healing cycles<sup>33,34</sup> Quite surprisingly, in the open literature, only a small number of papers concerning the self-healing properties of thermoplastic matrices can be found. One of the most studied thermoplastic materials is the so-called self-healable shape memory thermoplastic materials.<sup>35</sup> These materials are capable of reaching relatively high healing efficiency, but their mechanical properties are rather limited. Recently, Duarte et al.<sup>36</sup> utilized carbon fibers decorated with carbon quantum dots as reinforcement in poly(methyl methacrylate) (PMMA) composites. They demonstrated that the carbon dots on the surface of the carbon fibers provide reversible mechanisms of fiber-PMMA interaction, enabling thus the healing at the fiber/matrix interphase. In literature, self-healing thermoplastic matrices compounded with thermoplastic particles with low melting/softening points can be found, but they are mainly focused on elastomers or thermoplastic polyurethane (TPU).<sup>37,38</sup> Silva et al.<sup>39</sup> prepared a novel immiscible polymer blend with remarkable self-healing properties, based on poly(ethylene glycol-co-cyclohexane-1,4-dimethanol terephthalate) (PETG) and EMAA. They investigated the healing behavior of this blend through micro indentation tests, monitoring then the evolution of the regeneration. The blend containing 50/50 of the components was capable to restore the damage in just 30 s, however, the overall mechanical properties were rather low. Recently, our group explored the potentiality of polycaprolactone (PCL) as a healing agent in a polyamide 6 (PA6) matrix and the most promising results were obtained in impact mode configuration.<sup>40</sup>

Based on these considerations, this work aims to develop a PA6 thermoplastic matrix with thermal mending properties, thanks to the addition of different amounts of a cyclic olefinic copolymer (COC), utilized as thermoplastic healing agents. The potentiality of COC as a healing agent has been already proven by our group in thermosetting systems.<sup>15–19</sup> Furthermore, COC is characterized by elevated mechanical properties and a relatively low glass transition temperature,<sup>41–45</sup> which enables the healing process at relatively low temperatures, thus avoiding any geometrical deformation of the components. An in-depth rheological, microstructural, and thermo-mechanical characterization of the produced blends was carried out, while the healing efficiency of the produced systems was assessed through the comparison between the fracture toughness ( $K_{IC}$ ) of the virgin and

thermally healed materials, both in quasi-static and impact mode. In the future, these matrices could be potentially applied to develop novel multifunctional TPCs possessing intrinsic self-healing properties, that could be utilized as structural materials.

## 2 | MATERIALS AND METHODS

### 2.1 | Materials

The thermoplastic matrix used in this study was a Radilon S 24 E 100 NAT polyamide 6, provided by Radici Group SpA (Gandino, Italy) in form of polymer granules (density = 1.14 g/cm<sup>3</sup>, melting temperature = 220°C). The cyclic olefin copolymer (COC) selected as healing agent was Topas COC 9506F-500, supplied by TOPAS Advanced Polymers GmbH (Raunheim, Germany) in form of granules (density = 1.01 g/cm<sup>3</sup>, glass transition temperature = 65°C, norbornene content = 61 wt%).

### 2.2 | Sample preparation

Before processing, PA6 pellets were dried for 8 h in a vacuum oven at a temperature of 80°C, while COC pellets were dried in a ventilated oven at a temperature of 50°C for 8 h. PA6 and COC granules were manually mixed at different relative amounts and subsequently compounded through a Thermo Haake Rheomix 600 internal mixer equipped with counter-rotating rotors, operating at 60 rpm for 5 min at a temperature of 230°C. The obtained blends were then compression molded in a Carver hot-plate press at 235°C for 8 min, under an applied pressure of 1.9 MPa. In this way, square sheets 10 × 10 × 2 mm<sup>3</sup> were prepared. Thicker sheets having a thickness of 5 mm and the same lateral dimensions were also prepared for the evaluation of the fracture toughness of the blends. The produced samples were denoted as PA6\_x-COC, where “x” is the weight fraction of COC in the PA6 matrix. Table 1 summarizes the prepared compositions with the corresponding weight fractions of each constituent.

### 2.3 | Experimental techniques

#### 2.3.1 | Rheological properties

Rheological measurements were performed with an HR-2 Discovery Hybrid Rheometer (TA Instruments) in parallel plate configuration, the diameter of the plates was 25 mm, and a gap of 1.0 mm between the plates was

TABLE 1 List of the prepared blend samples.

Sample	PA6 content (wt%)	COC content (wt%)
PA6	100	0
PA6_5COC	95	5
PA6_10COC	90	10
PA6_20COC	80	20
PA6_30COC	70	30
PA6_50COC	50	50
PA6_75COC	25	75
COC	0	100

utilized. Frequency sweep experiments were carried out at 230°C in air, the frequency range was set from 0.05 to 600 rad/s at a strain amplitude of 1%. In this configuration, the trends of the storage modulus ( $G'$ ), loss modulus ( $G''$ ), and complex viscosity ( $\eta^*$ ) as a function of frequency were detected. At least three specimens were tested for each composition.

### 2.3.2 | Microstructural and chemical properties

Light microscope (LM) micrographs of the produced blends were acquired by embedding the specimens in cylindrical epoxy beads and analyzed with a CH-9435 Heerbrugg optical microscope (Heerbrugg). ImageJ<sup>®</sup> software (National Institutes of Health Campus, release 1.8) was used to measure the diameter of the COC domains inside the PA6 matrix. Field emission scanning electron microscopy (FESEM) images of the cryo-fractured and healed surfaces of the samples were acquired by using a Zeiss Supra 40 microscope, operating at an accelerating voltage of 3.5 kV. Prior to the observations, the specimens were sputtered with a Platinum-Palladium (80:20) conductive coating. Fourier transformed infrared (FT-IR) spectroscopy was performed in attenuated total reflectance (ATR) mode by using a Perkin-Elmer Spectrum One instrument (Perkin Elmer GmbH), equipped with a ZnSe crystal and operating in a wavenumber range 650–4000  $\text{cm}^{-1}$ . In order to reduce the signal-to-noise ratio, a hundred scans were collected for each spectrum (resolution 4  $\text{cm}^{-1}$ ).

### 2.3.3 | Thermal properties

Differential scanning calorimetry (DSC) tests were conducted through a Mettler DSC30 machine under a nitrogen flow of 100 mL/min, in a temperature range from

–20 to 250°C, at a heating/cooling rate of 10°C/min. All the specimens, with a weight of ~10 mg each, were subjected to a first heating scan, a cooling scan, and a second heating scan. In this way, the thermal transitions of both the constituents of the blends were measured, and in particular, the glass transition temperature ( $T_g$ ) of the COC, the melting temperature and enthalpy ( $T_m$ ,  $\Delta H_m$ ) of PA6, the crystallization temperature and enthalpy ( $T_c$ ,  $\Delta H_{cc}$ ) of PA6. Equation 1 shows how the degree of crystallinity ( $\chi$ ) of the PA6 phase in the blends was evaluated.

$$\chi = \frac{\Delta H_m - \Delta H_{cc}}{\Delta H_m^* \omega} \cdot 100, \quad (1)$$

where  $\Delta H_{cc}$  is the enthalpy of cold crystallization of the PA6,  $\Delta H_m^*$  is the enthalpy of melting of fully crystalline PA6, taken equal to 230 J/g,<sup>46</sup> and  $\omega$  is the weight fraction of PA6 in the blend. Thermogravimetric analysis (TGA) was performed through a Mettler TG50IR thermobalance (Mettler Toledo Inc.), testing samples of ~10 mg at 10°C/min from 35°C up to 700°C, under a nitrogen flow of 100 mL/min. This test allowed the calculation of the temperature associated with a mass loss of 1% ( $T_{1\%}$ ) and of 5% ( $T_{5\%}$ ), and of the temperature associated with the maximum mass loss rate ( $T_D$ ), considered as the peak of the mass loss derivative (DTG) curve.

### 2.3.4 | Mechanical properties

Quasi-static tensile tests were carried out at room temperature by using an Instron<sup>®</sup> 5969 tensile testing machine (ITW Test & Measurement and Equipment) equipped with a 1 kN load cell. The tests were performed on ISO 527 1BA specimens at a crosshead speed of 10 mm/min, and at least 10 specimens were tested for each composition. In this way, the determination of the maximum stress ( $\sigma_{max}$ ), and of the strain at break ( $\epsilon_b$ ) was performed. Elastic modulus ( $E$ ) was determined through tensile tests by using the same machine equipped with an Instron<sup>®</sup> 2620-601 extensometer, with a gauge length of 12.5 mm, at a crosshead speed of 0.25 mm/min. It was calculated as the secant modulus considering the stress levels associated with the strain values of 0.05% and 0.025%, as illustrated in the ISO-527 standard.

The fracture toughness of the blends was evaluated according to the procedure described in the ASTM D5045 standard. The tests were carried out on Single Edge Notched Bending (SENB) specimens, having dimensions of 44 × 10 × 5  $\text{mm}^3$ , an initial notch length of 5 mm, and a span length of 40 mm. At least 10 specimens were tested for each composition. Tests in quasi-static mode were performed in three-point bending configuration by

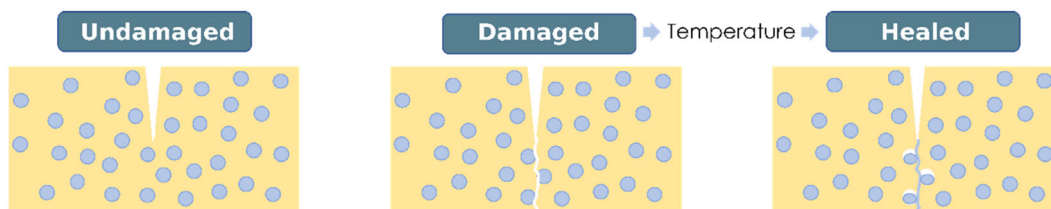


FIGURE 1 Schematic representation of the thermal mending process performed. [Color figure can be viewed at [wileyonlinelibrary.com](http://wileyonlinelibrary.com)]

using an Instron<sup>®</sup> 5969 electromechanical testing machine with a crosshead speed of 10 mm/min. Tests in impact mode were performed using a Charpy impact machine provided by CEAST, following the ISO 17281 standard, and the load–displacement curves were recorded using a tup extensometer in the hammer. A mass of the hammer equal to 0.5 kg, a starting angle of 60°, and an impact speed of 1.5 m/s were utilized. From the load–displacement curves, the maximum load sustained by the samples ( $P_{\max}$ ) was determined, and it was possible to determine the critical stress intensity factor ( $K_{IC}$ ), both in quasi-static and impact conditions, according to the expressions reported in Equation 2 and 3:

$$K_{IC} = \left( \frac{P_{\max}}{BW^{1/2}} \right) \cdot f(x), \quad (2)$$

$$f(x) = 6x^{1/2} 1.99 - x \left( \frac{(1-x)(2.15 - 3.93x + 2.7x^2)}{(1+2x)(1-x)^{3/2}} \right), \quad (3)$$

where,  $P_{\max}$  is the maximum load sustained by the samples,  $B$  is the thickness of the sample,  $W$  is the width of the samples, and  $f(x)$  is a calibration factor, where  $x = a/W$ , being  $a$  the notch length. Furthermore, accordingly to ASTM D5045 standard, from the integration of the load–displacement curves and the evaluation of system compliance, also the critical strain energy release rate ( $G_{IC}$ ) values in quasi-static mode were obtained, according to the expression reported in Equation 4:

$$G_{IC} = \frac{\Delta U}{BW\varphi} \quad (4)$$

where,  $\Delta U$  is the difference of the total energy absorbed by the sample and the energy absorbed in the indentation tests, and  $\varphi$  is an energy calibration factor, whose expressions is reported in Equation 5, 6, and 7:

$$\varphi = \frac{A + 18.64}{dA/dx}, \quad (5)$$

$$A = \left[ \frac{16x^2}{(1-x)^2} \right] \left[ 8.9 - 33.717x + 79.616x^2 - 112.952x^3 + 84.815x^4 - 25.672x^5 \right], \quad (6)$$

$$\frac{dA}{dx} = \left[ \frac{16x^2}{(1-x)^2} \right] \left[ -33.717 + 159.232x - 338.856x^2 + 339.26x^3 - 128.36x^4 \right] + \left[ \frac{32x}{(1-x)^3} \right] \left[ 8.9 - 33.717x + 79.616x^2 - 112.952x^3 + 84.815x^4 - 25.672x^5 \right]. \quad (7)$$

### 2.3.5 | Evaluation of the healing efficiency

After testing, a thermal mending process was performed to promote the intrinsic self-healing process in the prepared blends. Specifically, specimens broken in fracture toughness tests both under quasi-static and impact conditions were inserted in an iron vice with an applied pressure of 0.5 MPa and then heated in an oven at 140°C for 60 min. Figure 1 reports a schematization of the thermal mending process.

These parameters were selected after preliminary trials and on the basis of a previous paper of our group.<sup>40</sup> The selected temperature was higher than the  $T_g$  of COC and also enabled the macromolecular mobility of the healing agent within the PA6 matrix during the healing process. Before inserting the sample in the iron vice, a polytetrafluoroethylene (PTFE) film was inserted to limit the adhesion between the specimens and the vice. The healing process was performed only on neat PA6 and PA6\_30COC specimens. Neat PA6 was selected as a reference, while the PA6\_30COC sample was chosen for its

good mechanical properties. The healed specimens were tested again both in quasi-static and impact mode, and the fracture toughness of the healed specimens ( $K_{IC,Healed,i}$ ) was thus obtained. The healing efficiency ( $\eta_{KIC,i}$ ) for each specimen, was evaluated by using the expression reported in Equation 8:

$$\eta_{KIC,i} = \frac{K_{IC,Healed,i}}{K_{IC,Virgin,i}} \cdot 100. \quad (8)$$

### 3 | RESULTS AND DISCUSSIONS

#### 3.1 | Rheological properties

The rheological investigation of the produced blends was carried out to obtain more information about the processability of the blends and their miscibility.<sup>47</sup> Figure 2a,b reports the results obtained from the dynamic rheologic measurements on the prepared blends in terms of dynamic moduli, and complex viscosity. Dynamic moduli, that is, storage and loss modulus, represent the energy stored and consumed during the cyclic deformation process, respectively. Surprisingly, low-frequency  $G'$  values of the PA6\_xCOC samples are systematically higher in comparison to their individual components, especially in the case of PA6\_30COC, PA6\_50COC, and PA6\_75COC blends. A similar result was observed also in the work of Wang et al.<sup>48</sup> in which the effect of the addition of PBAT on the rheological properties of a PLA matrix was investigated. Zhao et al.<sup>49</sup> studied the rheological and crystallization properties of acrylonitrile butadiene styrene (ABS)/PA6 compatibilized blends. They also

reported an increment in the  $G'$  as a function of the ABS concentration in the blend.

As it is possible to notice in Figure 2b, the classic shear thinning behavior of polymeric materials can be detected,<sup>50</sup> that is, by increasing the deformation frequency the complex viscosity decreases.<sup>51</sup> As it is possible to notice in Figure 2b, at low frequencies, the complex viscosity of neat PA6 is significantly lower in comparison to the one of neat COC and, by increasing the COC content inside PA6, it is possible to notice an increase in the complex viscosity of the blends. It is possible to hypothesize that the presence of COC domains within the blends limits the motion of the PA6 macromolecules.<sup>52</sup>

The investigation of morphological changes in the prepared blends can also be performed by referring to Cole-Cole plots. By using this representation, the description of the viscoelastic properties of materials characterized by high relaxation time distribution can be obtained, thus highlighting phase separation phenomena within the blends.<sup>53</sup> At this aim, the imaginary viscosity ( $\eta''$ ) is reported as a function of real viscosity ( $\eta'$ ). By doing so, it is possible to see a smooth and semicircular arc of the curve, suggesting thus good compatibility among the constituents of the polymer blend in the melt state. On the other hand, if two different circular arcs or tails are observed, the existence of phase heterogeneity and immiscibility within the blend is demonstrated.<sup>54</sup> The investigation of the miscibility conditions in polymer blends in the molten state can also be performed through the Han plot, which shows a linear correlation in the plot of  $\log G'$  versus  $\log G''$ .<sup>55</sup> Through the Han plot, the compatibility of a polymer blend can be confirmed if the plotted curves are characterized by the same slope at different relative concentrations of the constituents.<sup>56,57</sup> On the other hand, if these curves are not characterized

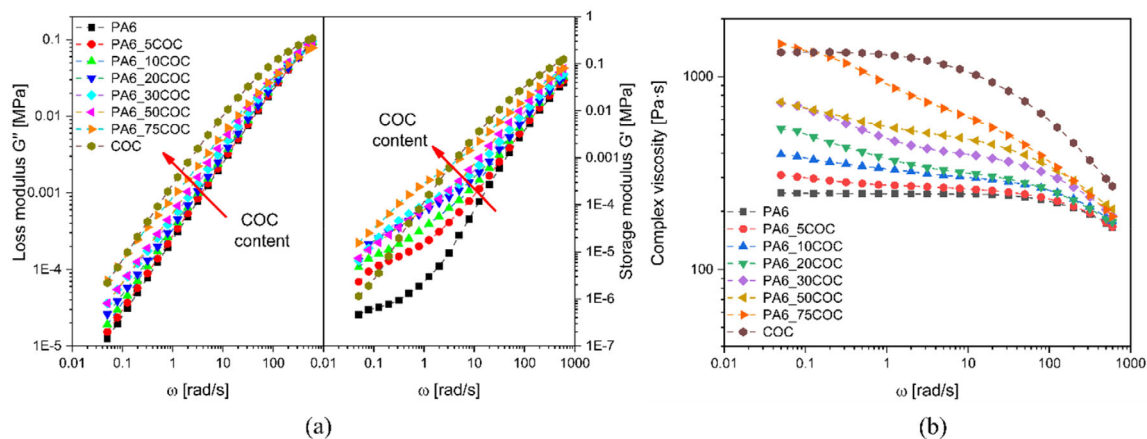


FIGURE 2 Dynamic rheological behavior of the produced PA6/COC blends. Trends of (a) storage and loss modulus, and of (b) complex viscosity as a function of the angular frequency. [Color figure can be viewed at [wileyonlinelibrary.com](http://wileyonlinelibrary.com)]

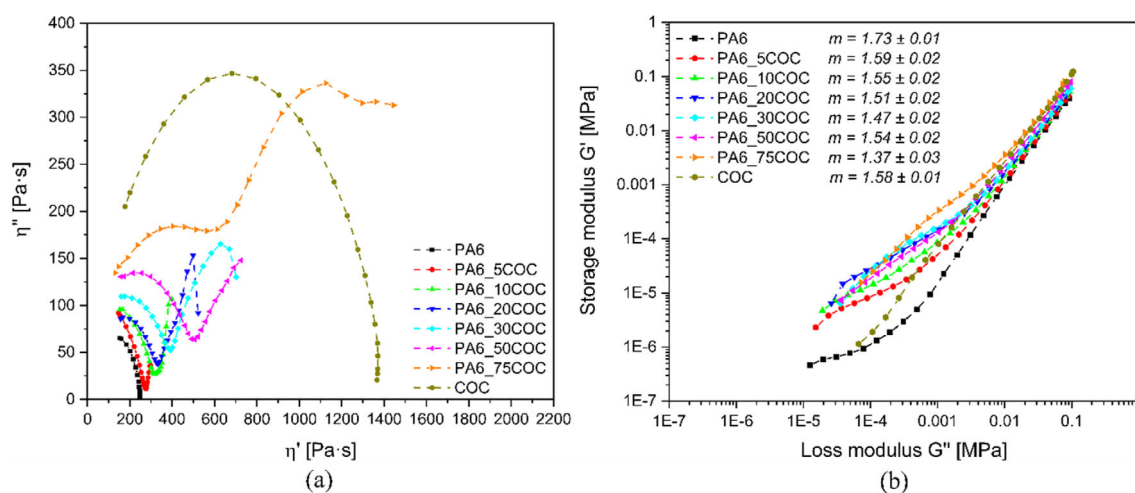


FIGURE 3 Rheological analysis of neat PA6, neat COC, and their blends: (a) Cole-Cole plot and (b) Han plot. [Color figure can be viewed at [wileyonlinelibrary.com](http://wileyonlinelibrary.com)]

by the same slope, the analyzed blend is considered to be immiscible.<sup>58,59</sup> The Cole-Cole plots of the neat matrices and their blends are reported in Figure 3a. As expected, the relaxation process of both neat PA6 and neat COC samples is described by a single circular arc, underlining the presence of a homogeneous composition, while an increase in the COC fraction in the blends leads to the appearance of two-stage relaxation phenomena, highlighting thus the immiscibility of the prepared blends. At high frequencies, the intrinsic relaxation of the major phase can be highlighted, while the relaxation process of the dispersed phase can be detected at low frequencies.<sup>60</sup> Figure 3b reports the Han plot of neat PA6, neat COC, and their blends. It can be noticed from these plots that the slope of the obtained is systematically different, and thus the blends can be considered immiscible.<sup>61,62</sup>

### 3.2 | Microstructural and chemical properties

Through the examination of the cross-section of the prepared blends through light microscopy it was possible to observe that, for COC contents up to 50%, the domains of COC distributed within the PA6 matrix were clearly distinguished, and the average diameter of COC domains tend to increase by increasing their concentration in the blends. Similar behavior was already observed by Gonzalez Núñez et al.<sup>63</sup> in PA6/LLDPE blends, where the diameter of the LLDPE domains increased with their relative amount. The average diameter of COC domains in the blend containing 5 wt% of COC is  $3.7 \pm 1.1 \mu\text{m}$  and their size increases up to  $23.4 \pm 5.1 \mu\text{m}$  for the PA6\_30COC blend. By increasing the

COC content at 75 wt%, a phase inversion occurs, and PA6 domains with an average diameter of  $24.7 \pm 4.7 \mu\text{m}$ , homogeneously dispersed within the COC matrix, were observed. In conclusion, from the obtained micrographs, it was possible to infer that the prepared blends are immiscible, and clear phase separation occurs over the entire investigated concentration range.

The phase morphology of PA6/COC blends was also investigated by FESEM, and Figure 4a–h reports the cryo-fractured surfaces of the prepared samples. In general, since the prepared blends undergo phase separation, a droplet-matrix type morphology can be detected.<sup>64</sup> Thus, blends containing 5 wt% (Figure 4b) and 10 wt% (Figure 4c) of COC present small COC domains, and also large cavities with clear contours, representing the COC dispersed domains pulled out from the PA6 matrix. Furthermore, Figure 4g reports the cryo-fractured surface of the PA6\_75COC blend, and even for this composition, it is possible to notice a rather poor interfacial adhesion between the two constituents. By increasing the COC content in the blends, the coalescence of the domains can be detected. In the literature,<sup>65,66</sup> it is reported that this specific morphology is often characterized by droplet breakup and coalescence phenomena. This is the reason why at elevated COC amounts the domains are homogeneously dispersed and their dimensions increased. The relatively high dimension of the dispersed COC domains coupled with the rather poor interfacial adhesion confirms the incompatibility of the produced blends. The poor compatibility between the constituents could also lead to a worsening of the mechanical properties of the blends. The results obtained from the morphological analyses are consistent with those obtained from the rheological analyses discussed in Section 3.1 (see Figure 3a,b).

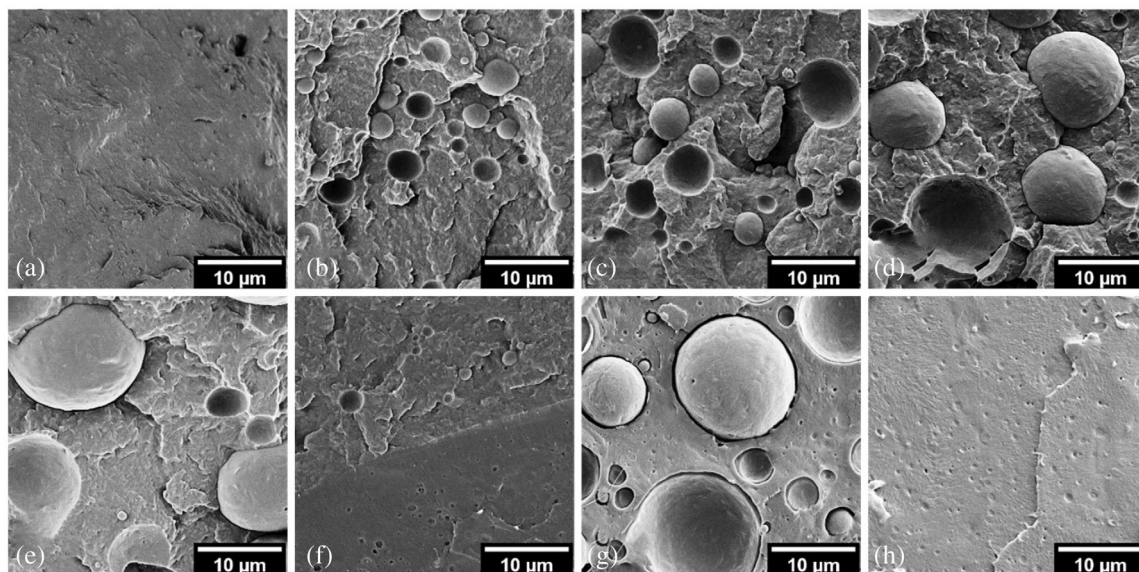


**FIGURE 4** SEM micrographs of the prepared PA6/COC blends. (a) PA6, (b) PA6\_5COC, (c) PA6\_10COC, (d) PA6\_20COC, (e) PA6\_30COC, (f) PA6\_50COC, (g) PA6\_75COC, and (h) COC.

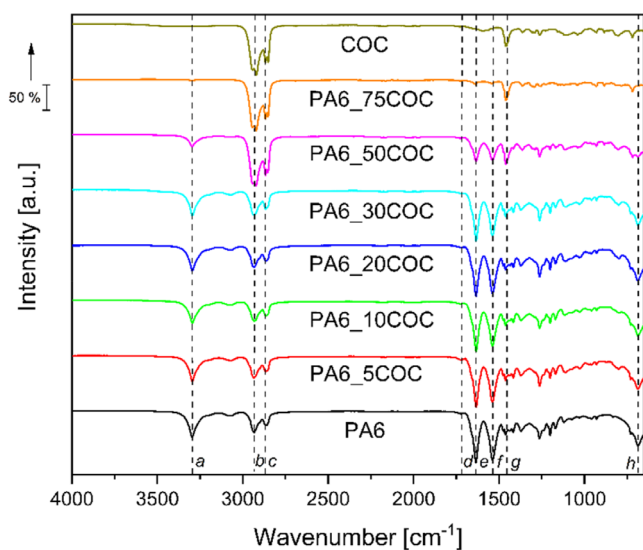
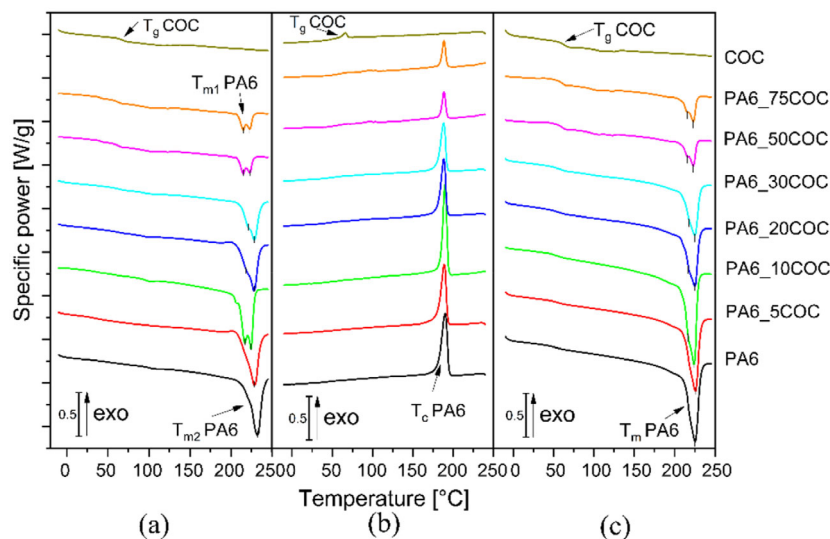


**FIGURE 5** ATR-FTIR spectra of the prepared PA6/COC blends. [Color figure can be viewed at [wileyonlinelibrary.com](http://wileyonlinelibrary.com)]

Figure 5a–c reports the FTIR spectra of neat PA6, neat COC, and of the prepared PA6/COC blends. The FT-IR spectrum of PA6 was extensively studied in the literature,<sup>67,68</sup> and the absorption bands located at 834, 929, 960, 1029, and 1200  $\text{cm}^{-1}$  suggest that the crystalline structure PA6 utilized in the present work is mainly constituted by the  $\alpha$ -crystalline phase.<sup>68,69</sup> According to Yeh et al.,<sup>70</sup> the band at 3293  $\text{cm}^{-1}$  (a) can be associated with the N–H stretching vibration of hydrogen-bonded N–H groups in the crystalline phase. The absorption band at 1634  $\text{cm}^{-1}$  (e) can be related to

C=O stretching vibrations while the mixed signals of C–N stretching and N–H in-plane bending vibration can be observed in the band at 1536  $\text{cm}^{-1}$  (f).<sup>71,72</sup> The two intense bands at 2931  $\text{cm}^{-1}$  (b) and at 2854  $\text{cm}^{-1}$  (c) can be related to the asymmetric and symmetric C–H stretching vibrations, respectively.<sup>73</sup> The bands located at 1475  $\text{cm}^{-1}$  and at 1416  $\text{cm}^{-1}$  derive from C–H<sub>2</sub> scissoring vibrations in the proximity of –NH and –C=O groups, respectively. The absorption bands at 1459  $\text{cm}^{-1}$  can be related to C–H<sub>2</sub> scissoring and the one at 1372  $\text{cm}^{-1}$  can be correlated to the twisting vibrations.<sup>74</sup> In addition, at 1433  $\text{cm}^{-1}$  (g) is located a band corresponding to the bending vibration of the CH<sub>2</sub> group near to the nitrogen atoms of the amide, indicating a rotational deviation of the –CH<sub>2</sub>–CONH–CH<sub>2</sub>– group from the ideal trans conformation. Moreover, the band located at 1167  $\text{cm}^{-1}$  can be associated with the vibrations of the N–C–O group.<sup>75</sup> Regarding the FT-IR spectrum of COC, the absorption peaks related to the ring deformation of norbornene units can be observed, since it is a copolymer of norbornene and ethylene. Thus, the characteristic bands at 1459, 1596, and 1639  $\text{cm}^{-1}$ , represent the C–H vibrations of the methylene group, the ring deformation of norbornene, the ethylene-norbornene conjugation, respectively. As it is possible to notice from these spectra, no interactions between COC and PA6 phases can be detected, and the characteristic peaks of COC can only be detected when its concentration in the blends is relatively high (i.e., 50 and 75 wt%). A possible explanation of this phenomenon can be attributed to the microstructure of the prepared blends and to the penetration depth of the FTIR technique. Being the COC domains homogeneously

**FIGURE 6** DSC thermograms of the produced PA6/COC blends. (a) First heating scan, (b) cooling scan, and (c) second heating scan. [Color figure can be viewed at [wileyonlinelibrary.com](http://wileyonlinelibrary.com)]



dispersed in the PA6 matrix, the outer surface of the specimens is composed of PA6, and the probability of detecting the signals of COC domains is thus rather low. Furthermore, the ATR-FTIR used in this work has a penetration depth of approximately 2  $\mu\text{m}$ , and therefore, by looking at the microstructure of the prepared blends (Figure 4a–h), it is clear the difficulty to detect COC signals. In any case, the absence of any shift for both PA6 and COC signals in FT-IR spectra of the blends confirms the immiscibility of the two polymer phases over the whole range of investigated compositions.

### 3.3 | Thermal properties

Figure 6 reports the DSC thermograms of neat PA6, neat COC, and of the prepared blends, while the most relevant results are summarized in Table 2. PA6 has a melting temperature of 230.6°C, while its glass transition temperature ( $T_g$ ) cannot be detected. The  $T_g$  of PA6 depends on several parameters, such as the moisture content, the crystallinity degree,<sup>76</sup> and the rigid amorphous phase amount.<sup>77</sup> Thus, considering the fact that the sample is characterized by a relatively high crystallinity (about 30%), the  $T_g$  signal is probably too weak to be detected. Regarding neat COC, it is fully amorphous and is characterized by a  $T_g$  of 65.0°C, in perfect agreement with the technical datasheet given by the company.

Furthermore, from the reported thermograms, it is possible to appreciate that there is no interaction between PA6 and COC since the  $T_g$  of COC is not affected by the presence of PA6. Interestingly, by looking at the melting peak of the PA6 phase, double melting phenomena arise when COC is blended with PA6. One of the most important characteristics of PA6 is its ability to form polymorphic crystals and in particular, two important crystal forms can be

produced during melt processing. The first is the most stable  $\alpha$ -phase (with monoclinic cell) produced for low under-cooling, while the second, the less stable,  $\gamma$ -mesophase (with pseudo-hexagonal cell) can be produced for high under-cooling.<sup>78</sup> By performing the peak deconvolution of the melting peaks, it was possible to extrapolate the two different melting temperatures of the  $\alpha$ -phase ( $T_{m2}$ ) and  $\gamma$ -phase ( $T_{m1}$ ). The addition of COC to the PA6 matrix may hinder the formation of more stable crystallites and therefore, during the cooling phase, less stable crystallites can be formed. The crystallization behavior of PA6, in terms of  $T_c$  and  $\Delta H_c$ , is affected by the presence of COC. Similar results were obtained by Soheli et al.<sup>79</sup> in their work on PA6/ABS blends. They noticed a  $T_c$  of the produced blends slightly lower than PA6, which may be caused by the increment in the melt viscosity of the blends by increasing the ABS concentration. In the work of Sridhara et al.,<sup>80</sup> the crystallinity of PA6 slightly decreased upon the addition of cellulose nanofibers (CNF), because these nanofillers affected the mobility of the polymeric chains. However, as it is possible to notice from Table 2, the position of the melting peaks related to the  $\alpha$ -phase and  $\gamma$ -phase, and the overall crystallinity of PA6 are only slightly affected by the COC content. Therefore, also DSC analysis highlights the immiscibility of the two polymer phases in the prepared blends at all the investigated compositions.

Figure 7a,b reports the TGA thermograms and the derivative thermogravimetric (DTG) curves of neat PA6, neat COC, and on the prepared blends, while the main results are reported in Table 3. The residual mass at 700°C for each of the tested specimens is zero, indicating a complete thermal degradation of the samples. It is worthwhile to underline the fact that there is no weight loss above 100°C for all the produced blends, and thus it can be concluded that the produced blends are completely dry. On the basis of the obtained

TABLE 2 Results of the DSC tests on the prepared PA6/COC blends.

First heating scan					
Sample	T <sub>g</sub> COC (°C)	T <sub>m1</sub> PA6 (°C)	T <sub>m2</sub> PA6 (°C)	ΔH <sub>m,PA6</sub> (J/g)	χ PA6 (%)
PA6	-	-	230.6	56.9	24.7
PA6_5COC	-	-	225.8	51.6	23.6
PA6_10COC	63.4	217.0	223.8	50.4	26.6
PA6_20COC	64.1	219.3	226.2	44.0	23.9
PA6_30COC	64.0	221.5	224.7	36.6	22.7
PA6_50COC	63.0	215.2	222.6	27.8	24.2
PA6_75COC	63.2	214.8	222.6	15.3	26.5
COC	65.0	-	-	-	-
Cooling scan					
Sample	T <sub>g</sub> COC (°C)	T <sub>c</sub> PA6 (°C)	ΔH <sub>c,PA6</sub> (J/g)	χ PA6 (%)	
PA6	-	192.8	67.1	29.2	
PA6_5COC	-	190.1	65.8	30.1	
PA6_10COC	-	191.6	66.1	31.9	
PA6_20COC	-	189.2	54.7	29.7	
PA6_30COC	-	189.4	45.5	28.3	
PA6_50COC	-	189.5	34.5	30.4	
PA6_75COC	-	189.4	17.9	31.2	
COC	64.1	-	-	-	
Second heating scan					
Sample	T <sub>g</sub> COC (°C)	T <sub>m1</sub> PA6 (°C)	T <sub>m2</sub> PA6 (°C)	ΔH <sub>m,PA6</sub> (J/g)	χ PA6 (%)
PA6	-	-	223.5	67.1	29.2
PA6_5COC	61.0	-	224.5	65.6	30.0
PA6_10COC	62.7	218.6	223.1	64.5	31.1
PA6_20COC	62.3	219.4	224.7	54.7	29.7
PA6_30COC	61.0	219.3	224.0	45.6	28.3
PA6_50COC	59.6	217.1	223.4	31.9	27.8
PA6_75COC	60.3	217.1	222.8	15.9	27.7
COC	61.3	-	-	-	-

experimental results, it can be concluded that COC is characterized by superior thermal stability in comparison to PA6, and PA6 samples blended with COC show an improved thermal degradation resistance. Both the T<sub>5%</sub> and T<sub>D</sub> tend to increase by increasing the COC concentration, going from 394.5 and 463.5°C for neat PA6 up to 458.7 and 485.7°C for neat COC, respectively.

### 3.4 | Mechanical properties

Figure 8a–d reports the representative stress–strain curves and the trends of elastic modulus (E), maximum stress (σ<sub>max</sub>), and elongation at break (ε<sub>b</sub>) of the prepared

blends, obtained from quasi-static tensile tests. From Figure 8a it is clear that all the prepared blends exhibit brittle behavior except for COC, which shows yielding phenomena.

The modelization of the elastic modulus of the prepared blends was performed by using the Maxwell-Eucken (ME) model. This model is able to predict the mechanical properties of a blend characterized by the droplet-matrix morphology.<sup>81</sup> The expression of the ME model is reported in Equation 9:

$$E_m = \frac{E_1 \vartheta_1 + E_2 \vartheta_2 \frac{3E_1}{2E_1 + E_2}}{\vartheta_1 + \vartheta_2 \frac{3E_1}{2E_1 + E_2}} \quad (9)$$

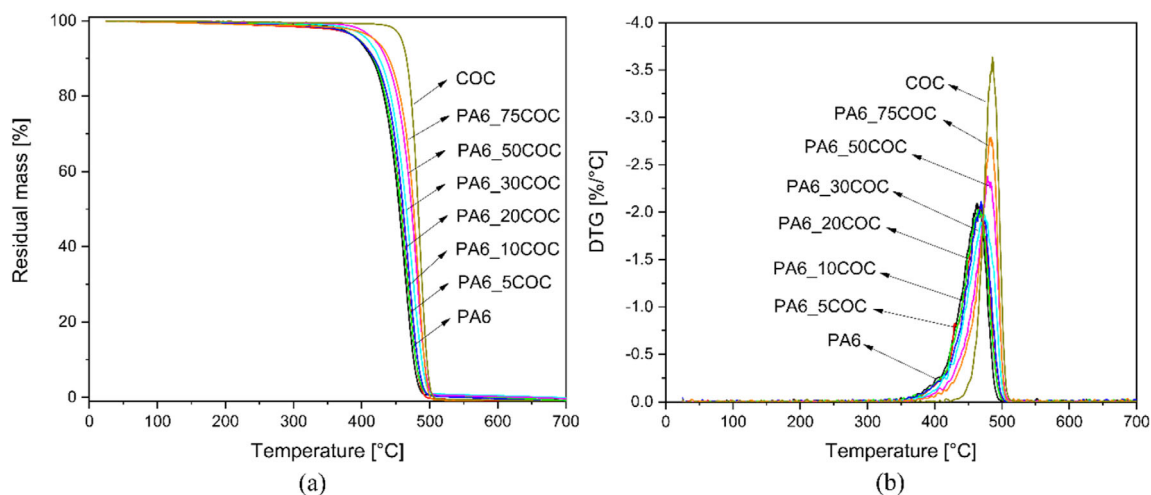


FIGURE 7 TGA tests on the prepared PA6/COC blends. (a) Residual mass, and (b) mass loss derivative curves. [Color figure can be viewed at [wileyonlinelibrary.com](http://wileyonlinelibrary.com)]

TABLE 3 Results of the TGA analysis performed on the prepared PA6/COC blends.

Sample	T <sub>1%</sub> (°C)	T <sub>5%</sub> (°C)	T <sub>D</sub> (°C)
PA6	318.0	394.5	463.5
PA6_5COC	229.3	396.2	466.7
PA6_10COC	295.8	396.3	464.3
PA6_20COC	271.0	395.2	468.8
PA6_30COC	344.3	408.8	474.3
PA6_50COC	372.2	418.7	478.5
PA6_75COC	238.2	419.7	483.7
COC	429.2	458.7	485.7

where  $E_m$  is the modulus of the blend,  $E_i$  and  $\vartheta_i$  are the moduli, and the volume fraction of phase  $i$ , respectively.

Theoretically speaking, the application of the ME model implies that the blend is composed of small spheres dispersed within a continuous matrix, and provides a good approximation of the mechanical properties of the blends for limited volume fraction of the dispersed phase. However, in the present case, the trend of the mechanical properties of the produced blends is lower than the ME model prediction over the whole range of the investigated compositions. This discrepancy can be probably ascribed to the lack of adhesion between the two polymer phases. The elastic modulus decreases from  $3.1 \pm 0.2$  GPa for neat PA6 to  $2.5 \pm 0.2$  GPa for PA6\_30COC, the maximum stress decreases from  $77.2 \pm 3.6$  MPa for neat PA6 to  $40.4 \pm 1.9$  MPa for PA6\_30COC (relative drop of 48%), and the elongation at break decreases from  $8.9 \pm 2.0\%$  for neat PA6 to  $3.1 \pm 0.1\%$  for PA6\_30COC (relative drop of 65%). The

mechanical properties of an immiscible polymer blend can be strongly influenced by various phenomena, such as cavitation during the deformational process, decohesion at the interfaces of the two constituents, and also the lower mechanical properties of the second component.<sup>82</sup> From the Cole-Cole plot (Figure 3a), the appearance of two-stage relaxation phenomena suggests the immiscibility of the prepared blends. Moreover, from the SEM micrographs (Figure 4e), it is possible to appreciate the lack of interfacial adhesion between the dispersed COC domains and the PA6 matrix. Therefore, the limited interfacial interaction between PA6 and COC clearly explains the observed decrease in the mechanical properties of the prepared blends. For instance, Castro et al.<sup>83</sup> produced PA6/ABS blends and they also found a decrease in the mechanical properties by adding ABS to neat PA6. They improved the mechanical properties of the blends by performing reactive compatibilization by using methyl methacrylate-co-maleic anhydride (MMA-MA). Sridhar et al.<sup>84</sup> investigated PA6/polypropylene (PP) blends to improve both the strength and toughness. For low PP contents, they noticed a positive impact on the overall mechanical properties. However, at high PP concentrations, the mechanical properties decreased due to the lack of interfacial adhesion. Through the introduction of PP-g-maleic anhydride as a compatibilizer, a partial restoration of the mechanical properties was observed.

Concerning the fracture behavior of the prepared blends under quasi-static mode, Figure 9a,b reports the trends of  $K_{IC}$  and  $G_{IC}$  as a function of the volume fraction of COC. All the tested specimens completely fulfilled the elasticity requirements of ASTM D5045 standard. The obtained  $K_{IC}$  value for neat PA6 ( $2.3$  [MPa·m<sup>1/2</sup>]) is in

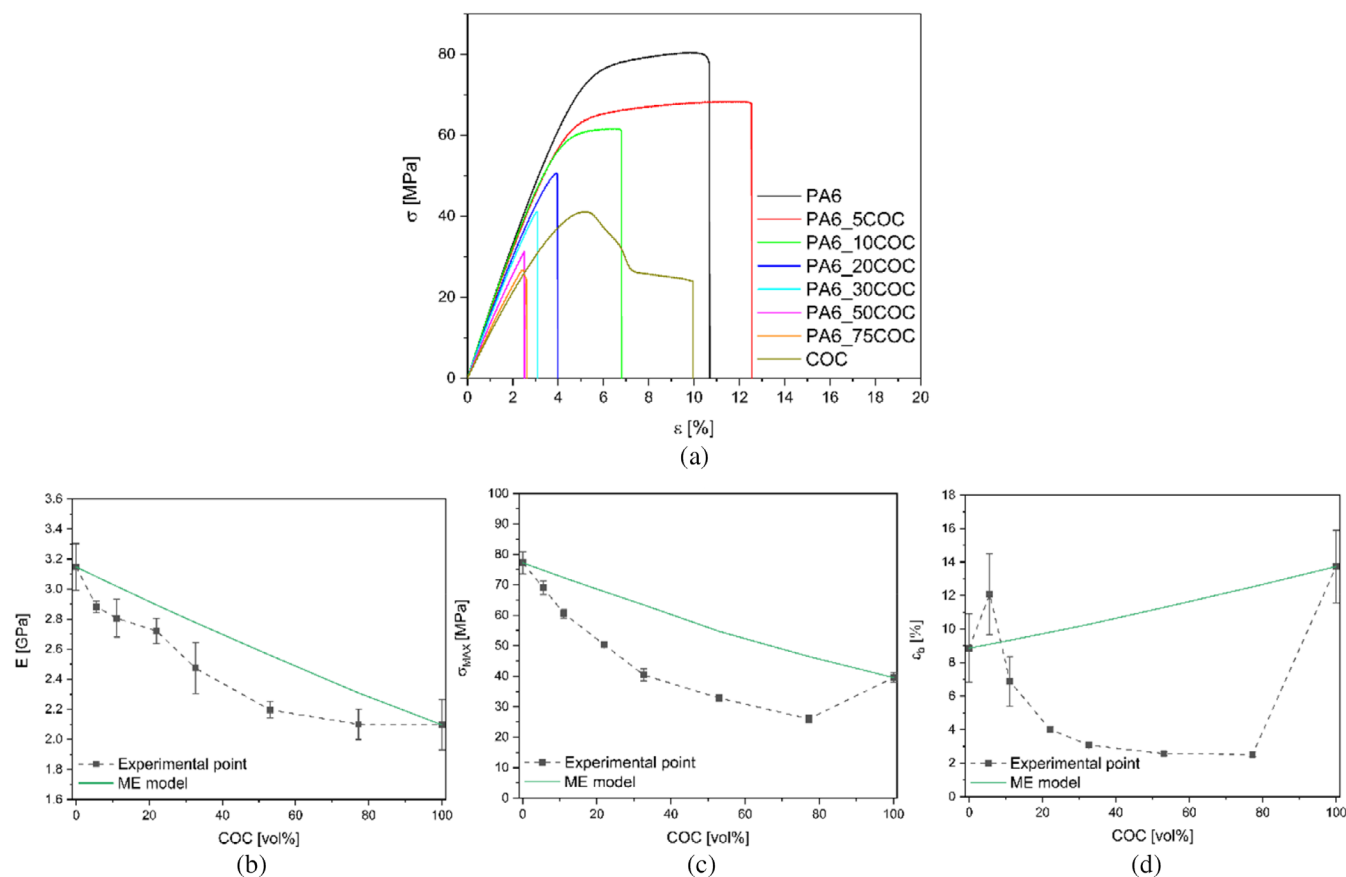


**FIGURE 8** Results of quasi-static tensile tests on the prepared PA6/COC blends. (a) Representative stress–strain curves, trends of (b) elastic modulus, (c) of the maximum stress, and (d) of the elongation at break as a function of the COC content. [Color figure can be viewed at [wileyonlinelibrary.com](http://wileyonlinelibrary.com)]

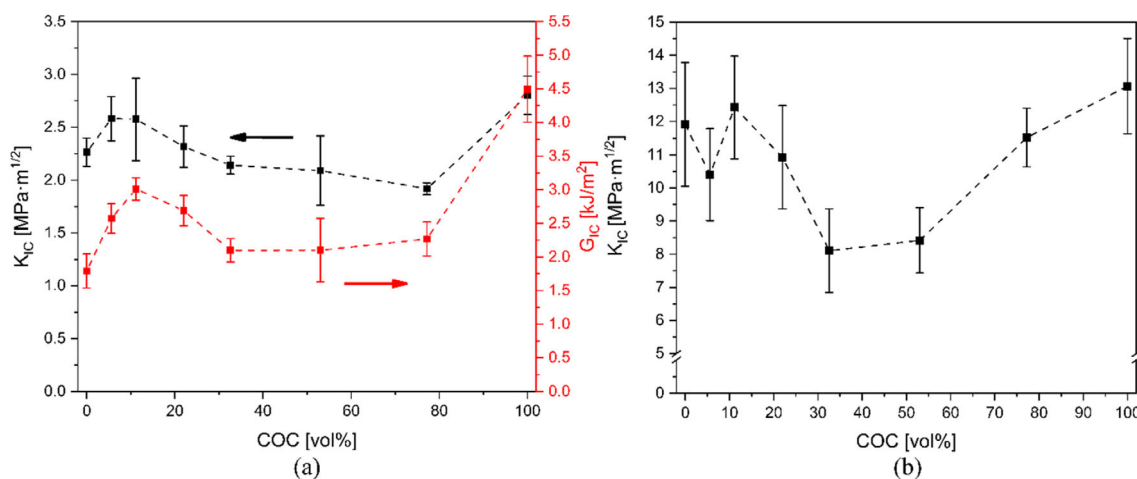


**FIGURE 9** Fracture behavior of the prepared PA6/COC blends. (a) Critical stress intensity factor ( $K_{IC}$ ), and critical strain energy release rate ( $G_{IC}$ ) in quasi-static mode, (b) critical stress intensity factor ( $K_{IC}$ ) in impact mode. [Color figure can be viewed at [wileyonlinelibrary.com](http://wileyonlinelibrary.com)]

perfect agreement with the typical values reported in the literature,<sup>85</sup> while neat COC reports a higher fracture toughness value (2.7 [MPa·m<sup>1/2</sup>]). It is very interesting to

notice that, for a concentration of COC as low as 5 and 10 wt%, the value of  $K_{IC}$  slightly increases up to 2.6 (MPa·m<sup>1/2</sup>). On the other hand, by increasing the COC

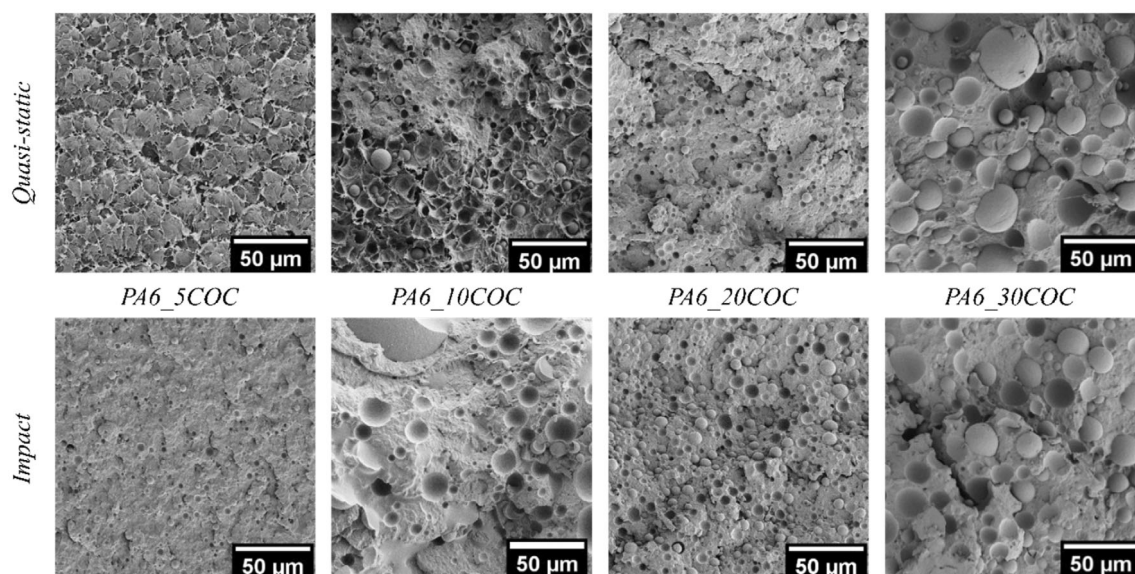


**FIGURE 10** SEM micrographs of the tested SENB specimens of the blends containing up to 30 wt% of COC in quasi-static mode and impact mode.

content up to 30 wt%,  $K_{IC}$  slightly decreases to  $2.1 \pm 0.1$  ( $\text{MPa}\cdot\text{m}^{1/2}$ ). A similar trend can be observed for  $G_{IC}$  values. The increment in the  $K_{IC}$  and in the  $G_{IC}$  values for low COC concentrations can be reconducted to a particular toughening mechanism, that is, the formation of microvoids through cavitation or particle debonding.<sup>86</sup> Through particle debonding, an alteration of the stress state in the surrounding matrix is possible, enabling the matrix to yield at moderate stress levels, even under plane-strain conditions, and thus initiating plastic deformation inside the matrix.<sup>87</sup> The generation of microvoids through particles debonding converts the material, in the proximity of the deformation zone, into a porous solid starting from a continuous solid, determining a slight increment in the absorbed fracture energy.<sup>88</sup> On the other hand, this mechanism is also responsible for the reduction in the overall mechanical properties of the produced blends, as reported in Figure 8a–d. In any case, it can be generally concluded that the fracture toughness under quasi-static conditions of the PA6 is not negatively affected by the COC introduction, even if the two polymers are immiscible. Figure 9 b reports the  $K_{IC}$  values obtained from fracture toughness tests in impact mode on the prepared blends as a function of the volume fraction of COC. It is interesting to notice that, at low COC concentrations, the values of  $K_{IC}$  are comparable with those of neat PA6, while a decrease can be observed at higher COC concentrations. A similar trend was also observed in quasi-static mode. Even in this case, the decrease in the  $K_{IC}$  values at elevated COC amounts can be attributed to the lack of adhesion between the COC and the PA6 matrix. Moreover, the  $K_{IC}$  values evaluated

in impact mode are significantly higher than those reported in quasi-static mode. A possible reason for this discrepancy can be reconducted to the different deformation speed, which may lead to the activation of different fracture mechanisms. Further efforts should be made in the future to explain this result.

In order to better understand the fracture mechanism that occurred both in quasi-static and impact mode, SEM micrographs of the tested SENB specimens are reported in Figure 10. The debonding process is fundamental for the improvement of the toughness since it allows the matrix to deform plastically through a void growth mechanism subdivided into particle debonding, void nucleation, growth, and crazing.<sup>89</sup> In quasi-static mode, the surface of the tested specimens with a COC concentration as low as 5 or 10 wt% results irregular, partially plastically deformed, and the voids formed during the particle debonding process are visible. Thus, more energy is required by the crack for its propagation.<sup>90</sup> This morphology explains the improvement in the fracture toughness of the prepared blends at limited COC amounts. For higher COC concentrations, it is still possible to notice the occurrence of the debonding mechanisms since there is a small gap between the COC domains and the PA6 matrix, which means that the matrix was slightly plastically deformed. On the other hand, at higher testing speeds, the toughening mechanism of particle debonding does not occur since there is no plastic deformation and there is no gap between the COC domains and the PA6 matrix.<sup>91</sup> For this reason, no improvement at low COC concentration occurs in the  $K_{IC}$  in impact mode. At higher values of COC concentration, it is possible to

**TABLE 4** Evaluation of the healing efficiency in quasi-static and impact mode for the PA6\_30COC blend.

Quasi-static mode		
Sample	$K_{IC}$ (MPa·m <sup>1/2</sup> )	HE (%)
PA6	2.26 ± 0.13	-
PA6_H	0	0
PA6_30COC	2.11 ± 0.01	-
PA6_30COC_H	0.24 ± 0.05	11.4 ± 2.1
Impact mode		
Sample	$K_{IC}$ (MPa·m <sup>1/2</sup> )	HE (%)
PA6	11.91 ± 2.02	-
PA6_H	0	0
PA6_30COC	7.80 ± 1.99	-
PA6_30COC_H	2.71 ± 1.45	34.7 ± 9.3

notice the detrimental effect of the immiscibility since there is rather no continuity in the matrix and thus the crack can easily go through the materials.

### 3.5 | Evaluation of the healing efficiency

Table 4 reports the  $K_{IC}$  values obtained in quasi-static and impact mode for the blend containing 30 wt% of COC, before and after the healing process. By looking at the obtained results, the healing efficiency in quasi-static mode is 11.4 ± 2.1%, while in impact mode is 34.7 ± 9.3%. Moreover, since the healing efficiency of neat PA6 is 0%, only the dispersed COC phase is considered able to repair the specimens during the healing procedure, partially restoring thus the pristine mechanical properties. Interestingly, the overall healing efficiency evaluated in impact mode is significantly higher with respect to that observed in quasi-static mode.

The reason behind this phenomenon might be related to the fact that different testing speeds generate different fracture surface morphology. The fracture surfaces of the specimen tested in quasi-static mode are less planar than those observed in impact conditions (see Figure 10), the COC can thus easily flow and fill the crack in the impact-tested samples in a more efficient manner. In order to better understand the difference between the healing efficiency values observed in quasi-static and impact mode, it could be interesting to compare the microstructural features of the PA6\_30COC blend before and after the healing process. Thus, Figure 11 reports the SEM micrographs of the fracture surfaces of PA6\_30COC specimens tested in quasi-static and impact mode, before and after the healing process. Regardless of the testing speed, the fracture

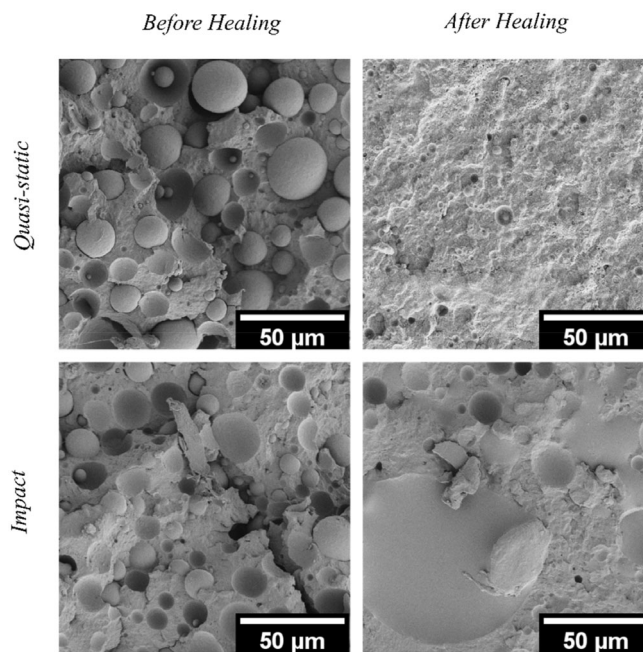


**FIGURE 11** SEM micrographs of the fracture surface of the PA6\_30COC blend before and after the healing process (tested both in quasi-static and impact conditions).

surfaces after the healing process have a much smoother appearance. The smooth surface of the impact specimen still presents several voids due to the detachment of COC domains, but it is possible to notice a thin COC layer that covers the majority of the cracked surface. On the other hand, in the specimen tested in quasi-static mode, only in certain zones of the surface it is possible to notice a homogeneous COC layer, while in the rest of the specimen only PA6 can be detected. The COC domains softened during the healing process and were capable of filling the crack in a more efficient way in impact mode, given the fact that the fracture surface was more planar. However, being the adhesion between COC domains and PA6 matrix very poor, the healing efficiency of the prepared PA6/COC systems is therefore rather limited. A direct comparison with the existing literature works is quite complex, given the particular healing mechanism that is occurring in our materials. Nevertheless, several works based on dynamic electrostatic interactions and hydrogen bonds,<sup>92</sup> dynamic bonds,<sup>93</sup> and double self-cross-linking networks<sup>94</sup> have been published and the reported healing efficiency values reached a level as high as 93%. It can be hypothesized that the healing efficiency obtained in the present system could be further enhanced through the addition of a proper compatibilizer, thus improving the interphase between COC and PA6. Moreover, also the addition of carbon nanofibers or carbon nanotubes (CNT) could provide nanofiller-induced compatibilization, which could boost the healing capability of these blends.<sup>95</sup>

## 4 | CONCLUSIONS

In this work, an investigation of the intrinsic self-healing behavior of a thermoplastic healing agent dispersed in a thermoplastic matrix was carried out. At this aim, COC was blended in various concentrations with PA6 through melt mixing and subsequent hot pressing. A comprehensive rheological, microstructural, and thermo-mechanical analysis was performed to obtain a full characterization of the produced blends. The evaluation of the healing efficiency of the most promising compositions was performed by comparing  $K_{IC}$  values before and after the thermal mending process, performed at 140°C.

From the rheological analysis, an increment in the complex viscosity was reported by increasing the COC content in the blends, and both Cole-Cole plot and Han-plot suggested the immiscibility of the COC/PA6 blends. The formation of a droplets-matrix morphology and the limited interfacial adhesion between the constituents was confirmed by LM and SEM micrographs. The immiscibility of the blends was detrimental to their quasi-static mechanical properties. The droplet-matrix morphology enhanced the  $K_{IC}$  in quasi-static mode at low COC contents, while at high COC concentrations, the  $K_{IC}$  decreased, and a similar trend was also observed in impact mode. The healing efficiency of the blends containing 30 wt% of COC in quasi-static mode was  $11.4 \pm 2.1\%$ , while in impact mode was  $34.7 \pm 9.3\%$ . The relatively low values of the healing efficiency were caused by the rather poor adhesion between COC and PA6. The limited value of the obtained healing efficiency in comparison to other systems, such as epoxy/PCL blends, may be ascribed to the different fracture morphology, characterized by a planar profile and a more even distribution of the healing agent. However, the potentiality of COC as a healing agent was demonstrated, as it was able to fill the cracks during the healing process, especially in impact-tested specimens.

The feasibility of producing a thermoplastic matrix possessing intrinsic self-healing properties at relatively low temperatures was thus demonstrated. These materials could be potentially exploited in the future as matrices for thermoplastic structural composites with self-healing capability. A possible improvement in the self-healing potential of these systems could be obtained by introducing suitable compatibilizers, in order to improve the adhesion between COC domains and the PA6 matrix.

### AUTHOR CONTRIBUTIONS

**D. Perin:** Conceptualization (lead); data curation (lead); formal analysis (lead); investigation (lead); methodology (lead); software (lead); validation (lead); writing – original draft (lead); writing – review and editing (equal).

**A. Dorigato:** Conceptualization (equal); funding acquisition (equal); project administration (lead); resources (equal); supervision (lead); writing – review and editing (equal). **A. Pegoretti:** Funding acquisition (equal); project administration (equal); supervision (equal); writing – review and editing (equal).

### CONFLICT OF INTEREST STATEMENT

The authors declare no conflict of interest.

### ACKNOWLEDGMENT

Open Access Funding provided by Università degli Studi di Trento within the CRUI-CARE Agreement.

### FUNDING INFORMATION

This research received no specific grant from any funding agency in the public, commercial, or not-for-profit sectors.

### DATA AVAILABILITY STATEMENT

The data that support the findings of this study are available from the corresponding author upon reasonable request.

### ORCID

D. Perin  <https://orcid.org/0000-0002-6248-2012>

A. Pegoretti  <https://orcid.org/0000-0001-9641-9735>

### REFERENCES

- [1] R. Hsissou, R. Seghiri, Z. Benzekri, M. Hilali, M. Rafik, A. Elharfi, *Compos. Struct.* **2021**, 262, 113640.
- [2] S. Fafenrot, M. Korger, A. Ehrmann, in *Mechanical and Physical Testing of Biocomposites, Fibre-Reinforced Composites and Hybrid Composites* (Eds: M. Jawaid, M. Thariq, N. Saba), Woodhead Publishing, Sawston, UK **2019**.
- [3] R.-M. Wang, S.-R. Zheng, Y.-P. Zheng, *Polymer Matrix Composites and Technology*. in (Eds: R.-M. Wang, S.-R. Zheng, Y.-P. Zheng), Woodhead Publishing, **2011**.
- [4] G. Das Neves Carneiro, C. C. António, *Int. J. Mech. Mater. Des.* **2019**, 15, 93.
- [5] T. Jollivet, C. Peyrac, F. Lefebvre, *Procedia Eng.* **2013**, 66, 746.
- [6] N. J. Kanu, E. Gupta, U. K. Vates, G. K. Singh, *Compos. A: Appl. Sci. Manuf.* **2019**, 121, 474.
- [7] S. van der Zwaag, E. Brinkman, *Self healing Materials: Pioneering Research in The Netherlands*, IOS Press Amsterdam, The Netherlands **2015**.
- [8] S. Utrera-Barrios, R. Verdejo, M. A. López-Manchado, M. Hernández Santana, *Mater. Horiz.* **2020**, 7, 2882.
- [9] M. Mobaraki, M. Ghaffari, M. Mozafari, in *Self-Healing Composite Materials* (Eds: A. Khan, M. Jawaid, S. N. Raveendran, A. M. Ahmed Asiri), Woodhead Publishing, Duxford, UK **2020**.
- [10] Y. Wang, D. T. Pham, in *Smart Polymer Nanocomposites: Energy Harvesting, Self-Healing and Shape Memory Applications* (Eds: D. Ponnamma, K. K. Sadasivuni, J.-J. Cabibihan,

- M. A.-A. Al-Maadeed), Springer International Publishing, Cham **2017**.
- [11] H. Ying, Y. Zhang, J. Cheng, *Nat. Commun.* **2014**, *5*, 3218.
- [12] S. Ji, W. Cao, Y. Yu, H. Xu, *Adv. Mater.* **2015**, *27*, 7740.
- [13] M. Burnworth, L. Tang, J. R. Kumpfer, A. J. Duncan, F. L. Beyer, G. L. Fiore, S. J. Rowan, C. Weder, *Nature* **2011**, *472*, 334.
- [14] A. Dorigato, D. Rigotti, A. Pegoretti, *Materials* **2020**, *13*, 819.
- [15] H. Mahmood, A. Dorigato, A. Pegoretti, *Express Polym Lett* **2020**, *14*, 368.
- [16] A. Dorigato, H. Mahmood, A. Pegoretti, *J. Appl. Polym. Sci.* **2021**, *138*, 49937.
- [17] R. C. Zovi, H. Mahmood, A. Dorigato, G. Fredi, A. Pegoretti, *Molecules* **2020**, *25*, 5347.
- [18] H. Mahmood, A. Dorigato, A. Pegoretti, *Materials* **2020**, *13*, 2165.
- [19] R. Cescato, D. Rigotti, H. Mahmood, A. Dorigato, A. Pegoretti, *Polymer* **2021**, *13*, 2723.
- [20] S. J. Garcia, *Eur. Polym. J.* **2014**, *53*, 118.
- [21] R. Bernatas, S. Dagreou, A. Despax-Ferreres, A. Barasinski, *Clean Eng. Technol* **2021**, *5*, 100272.
- [22] S. R. Yousefi, O. Amiri, M. Salavati-Niasari, *Ultrason. Sonochem.* **2019**, *58*, 104619.
- [23] S. R. Yousefi, H. A. Alshamsi, O. Amiri, M. Salavati-Niasari, *J. Mol. Liq.* **2021**, *337*, 116405.
- [24] S. R. Yousefi, M. Ghanbari, O. Amiri, Z. Marzhooseyni, P. Mehdizadeh, M. Hajizadeh-Oghaz, M. Salavati-Niasari, *J. Am. Ceram. Soc.* **2021**, *104*, 2952.
- [25] S. R. Yousefi, A. Sobhani, H. A. Alshamsi, M. Salavati-Niasari, *RSC Adv.* **2021**, *11*, 11500.
- [26] M. A. Mahdi, S. R. Yousefi, L. S. Jasim, M. Salavati-Niasari, *Int. J. Hydrog. Energy* **2022**, *47*, 14319.
- [27] T. S. Ghanta, S. Aparna, N. Verma, D. Purnima, *Polym. Eng. Sci.* **2020**, *60*, 1717.
- [28] P. Wang, L. Yang, Y. Zhou, S. Gao, T. Cao, S. Feng, P. Xu, Y. Ding, *Compos. Commun.* **2021**, *25*, 100738.
- [29] X. Cheng, D. Wang, H. Ke, Y. Li, Y. Cai, Q. Wei, *Compos. Commun.* **2022**, *30*, 101073.
- [30] I. F. Villegas, L. Moser, A. Yousefpour, P. Mitschang, H. E. N. Bersee, *J. Thermoplast. Compos. Mater.* **2012**, *26*, 1007.
- [31] S. Meure, D. Y. Wu, S. Furman, *Acta Mater.* **2009**, *57*, 4312.
- [32] S. J. Kalista, J. R. Pflug, R. J. Varley, *Polym. Chem.* **2013**, *4*, 4910.
- [33] R. J. Varley, D. A. Craze, A. P. Mouritz, C. H. Wang, *Macromol. Mater. Eng.* **2013**, *298*, 1232.
- [34] K. Pingkarawat, T. Bhat, D. A. Craze, C. H. Wang, R. J. Varley, A. P. Mouritz, *Polym. Chem.* **2013**, *4*, 5007.
- [35] J. Zhang, M. Huo, M. Li, T. Li, N. Li, J. Zhou, J. Jiang, *Polymer* **2018**, *134*, 35.
- [36] É. C. Duarte, R. L. Oréfice, *J. Appl. Polym. Sci.* **2021**, *138*, 49644.
- [37] X. Xu, P. Fan, J. Ren, Y. Cheng, J. Ren, J. Zhao, R. Song, *Compos. Sci. Technol.* **2018**, *168*, 255.
- [38] K. Yu, A. Xin, Z. Feng, K. H. Lee, Q. Wang, *J. Mech. Phys. Solids* **2020**, *137*, 103831.
- [39] P. A. P. Silva, A. B. da Silva, J. P. F. Santos, R. L. Oréfice, *J. Appl. Polym. Sci.* **2021**, *138*, 50148.
- [40] D. Perin, G. Odorizzi, A. Dorigato, A. Pegoretti, *Appl. Sci.* **2022**, *12*, 12357.
- [41] A. Dorigato, A. Pegoretti, C. Migliaresi, *J. Appl. Polym. Sci.* **2009**, *114*, 2270.
- [42] A. Pegoretti, A. Dorigato, A. Biani, M. Slouf, *J. Mater. Sci.* **2016**, *51*, 3907.
- [43] A. Dorigato, A. Pegoretti, L. Fambri, C. Lonardi, M. Slouf, J. Kolarik, *Express Polym Lett* **2011**, *5*, 23.
- [44] A. Biani, W. Bonani, *Express Polym Lett* **2016**, *10*, 977.
- [45] A. Dorigato, A. Biani, W. Bonani, A. Pegoretti, *J. Cell. Plast.* **2019**, *55*, 263.
- [46] C. Millot, L.-A. Fillot, O. Lame, P. Sotta, R. Seguela, *J. Therm. Anal. Calorim.* **2015**, *122*, 307.
- [47] S. S. Banerjee, A. K. Bhowmick, *J. Mater. Sci.* **2016**, *51*, 252.
- [48] X. Wang, S. Peng, H. Chen, X. Yu, X. Zhao, *Compos. Part B* **2019**, *173*, 107028.
- [49] D. Zhao, D. Yan, X. Fu, N. Zhang, G. Yang, *ACS Omega* **2020**, *5*, 15257.
- [50] A. J. Poslinski, M. E. Ryan, R. K. Gupta, S. G. Seshadri, F. J. Frechette, *J. Rheol.* **1988**, *32*, 703.
- [51] B. Tuna, H. Benkreira, *Polym. Eng. Sci.* **2019**, *59*, E25.
- [52] I. Butnaru, M. P. Fernández-Ronco, J. Czech-Polak, M. Heneczkowski, M. Bruma, S. Gaan, *Polymer* **2015**, *7*, 1541.
- [53] L. Cui, Z. Zhou, Y. Zhang, Y. Zhang, X. Zhang, W. Zhou, *J. Appl. Polym. Sci.* **2007**, *106*, 811.
- [54] A. Codou, A. Anstey, M. Misra, A. K. Mohanty, *RSC Adv.* **2018**, *8*, 15709.
- [55] C. D. Han, J. Kim, *J. Polym. Sci. B Polym. Phys.* **1987**, *25*, 1741.
- [56] D. Chopra, M. Kontopoulou, D. Vlassopoulos, S. G. Hatzikiriakos, *Rheol. Acta* **2002**, *41*, 10.
- [57] S. H. Jafari, P. Pötschke, M. Stephan, H. Warth, H. Alberts, *Polymer* **2002**, *43*, 6985.
- [58] K. Lamnawar, F. Vion-Loisel, A. Maazouz, *J. Appl. Polym. Sci.* **2015**, *2010*, 116.
- [59] F. Walha, K. Lamnawar, A. Maazouz, M. Jaziri, *Polymer* **2016**, *8*, 61.
- [60] L.-P. Li, B. Yin, Y. Zhou, L. Gong, M.-B. Yang, B.-H. Xie, C. Chen, *Polymer* **2012**, *53*, 3043.
- [61] Y. Zhang, M. Zuo, Y. Song, X. Yan, Q. Zheng, *Compos. Sci. Technol.* **2015**, *106*, 39.
- [62] H. Kwag, D. Rana, K. Cho, J. Rhee, T. Woo, B. H. Lee, S. Choe, *Polym. Eng. Sci.* **2000**, *40*, 1672.
- [63] L. G. Núñez, R. G. R. C. Vázquez-Fletes, P. Ortega-Gudiño, M. O. Vázquez-Lepe, D. Rodrigue, R. González-Núñez, *Polym. Eng. Sci.* **2021**, *61*, 1007.
- [64] I. Fortelný, J. Jůza, *Polymer* **2019**, *11*, 761.
- [65] A. Anstey, A. Codou, M. Misra, A. K. Mohanty, *ACS Omega* **2018**, *3*, 2845.
- [66] J. H. H. Rossato, H. G. Lemos, G. L. Mantovani, *J. Appl. Polym. Sci.* **2019**, *136*, 47075.
- [67] Q. Wu, X. Liu, L. A. Berglund, *Polymer* **2002**, *43*, 2445.
- [68] N. Vasanthan, D. R. Salem, *J. Polym. Sci. B Polym. Phys.* **2001**, *39*, 536.
- [69] B. John, M. Furukawa, *J. Polym. Res.* **2012**, *19*, 9764.
- [70] J. T. Yeh, W. Wei, F. C. Tsai, Y. C. Lai, *Adv. Mater. Res.* **2011**, *189-193*, 3031.
- [71] Y. Tian, H. Qin, X. Yang, C. Chi, S. Liu, *Mater. Lett.* **2016**, *180*, 200.
- [72] V. Krylova, N. Dukštienė, *Appl. Surf. Sci.* **2019**, *470*, 462.
- [73] N. M. Stark, L. M. Matuana, *Polym. Degrad. Stab.* **2004**, *86*, 1.

- [74] L. Jasinska, M. Villani, J. Wu, D. van Es, E. Klop, S. Rastogi, C. E. Koning, *Macromolecules* **2011**, *44*, 3458.
- [75] J. Maillo, P. Pages, E. Vallejo, T. Lacorte, J. Gacén, *Eur. Polym. J.* **2005**, *41*, 753.
- [76] Y. P. Khanna, W. P. Kuhn, W. J. Sichina, *Macromolecules* **1995**, *28*, 2644.
- [77] I. Kolesov, R. Androsch, *Polymer* **2012**, *53*, 4770.
- [78] E. Parodi, L. E. Govaert, G. W. M. Peters, *Thermochim. Acta* **2017**, *657*, 110.
- [79] M. A. Sohel, A. Mandal, A. Mondal, S. Pan, A. SenGupta, *J. Therm. Anal. Calorim.* **2017**, *129*, 1689.
- [80] P. K. Sridhara, F. Vilaseca, *Polymer* **2021**, *13*, 1495.
- [81] J. F. Wang, J. K. Carson, M. F. North, D. J. Cleland, *Polym. Eng. Sci.* **2010**, *50*, 643.
- [82] Z. Bartczak, A. Galeski, in *Polymer Blends Handbook* (Eds: L. A. Utracki, C. A. Wilkie), Springer Netherlands, Dordrecht **2014**.
- [83] L. D. C. Castro, A. D. Oliveira, M. Kersch, V. Altstädt, L. A. Pessan, *J. Appl. Polym. Sci.* **2016**, *133*, 133.
- [84] A. Sridhar, P. Doddipatla, *J. Appl. Polym. Sci.* **2019**, *136*, 47690.
- [85] M. Hasanpour, M. K. Razavi Aghjeh, M. Mehrabi Mazidi, B. Afsari, *Polym. Bull.* **2020**, *77*, 3767.
- [86] C. B. Bucknall, D. R. Paul, *Polymer* **2009**, *50*, 5539.
- [87] C. B. Bucknall, D. R. Paul, *Polymer* **2013**, *54*, 320.
- [88] A. S. Argon, R. E. Cohen, *Polymer* **2003**, *44*, 6013.
- [89] M.-K. Kim, H.-I. Kim, J.-D. Nam, J. Suhr, *Polymer* **2022**, *254*, 125082.
- [90] Z. Chen, Y. Zhou, Y. Wu, S. Liu, H. Huang, J. Zhao, *Compos. Sci. Technol.* **2019**, *181*, 107700.
- [91] A. Musteață, G. Pelin, M. Botan, A. Popescu, L. Deleanu, *Mater. Plast.* **2020**, *57*, 153.
- [92] X. Yu, H. Zhang, Y. Wang, X. Fan, Z. Li, X. Zhang, T. Liu, *Adv. Funct. Mater.* **2022**, *32*, 2204366.
- [93] Y. Wang, X. Yu, H. Zhang, X. Fan, Y. Zhang, Z. Li, Y.-E. Miao, X. Zhang, T. Liu, *Macromolecules* **2022**, *55*, 7845.
- [94] X. Feng, X. Li, L. Song, W. Zhao, S. Wang, *Compos. Commun.* **2022**, *35*, 101345.
- [95] X. Zhao, H. Wang, Z. Fu, Y. Li, *ACS Appl. Mater. Interfaces* **2018**, *10*, 8411.

**How to cite this article:** D. Perin, A. Dorigato, A. Pegoretti, *J. Appl. Polym. Sci.* **2023**, *140*(16), e53751. <https://doi.org/10.1002/app.53751>